Bioinspir. Biomim. **8** (2013) 046013 (15pp) doi:10.1088/1748-3182/8/4/046013

Understanding undulatory locomotion in fishes using an inertia-compensated flapping foil robotic device

Li Wen[1,2] **and George Lauder**[1]

[1] The Museum of Comparative Zoology, 26 Oxford St., Harvard University, Cambridge, MA 02138, USA
[2] School of Mechanical Engineering and Automation, Beihang University, Beijing, 100191, People's Republic of China

E-mail: liwen@buaa.edu.cn and glauder@oeb.harvard.edu

Received 21 August 2013
Accepted for publication 7 November 2013
Published 21 November 2013
Online at stacks.iop.org/BB/8/046013

Abstract
Recent advances in understanding fish locomotion with robotic devices have included the use of flapping foil robots that swim at a constant swimming speed. However, the speed of even steadily swimming live fishes is not constant because the fish center of mass oscillates axially throughout a tail beat cycle. In this paper, we couple a linear motor that produces controlled oscillations in the axial direction to a robotic flapping foil apparatus to model both axial and side to side oscillatory motions used by freely-swimming fishes. This experimental arrangement allows us to compensate for the substantial inertia of the carriage and motors that drive the oscillating foils. We identify a 'critically-oscillated' amplitude of axial motion at which the cyclic oscillations in axial locomotor force are greatly reduced throughout the flapping cycle. We studied the midline kinematics, power consumption and wake flow patterns of non-rigid foils with different lengths and flexural stiffnesses at a variety of axial oscillation amplitudes. We found that 'critically-oscillated' peak-to-peak axial amplitudes on the order of 1.0 mm and at the correct phase are sufficient to mimic center of mass motion, and that such amplitudes are similar to center of mass oscillations recorded for freely-swimming live fishes. Flow visualization revealed differences in wake flows of flexible foils between the 'non-oscillated' and 'critically-oscillated' states. Inertia-compensating methods provide a novel experimental approach for studying aquatic animal swimming, and allow instrumented robotic swimmers to display center of mass oscillations similar to those exhibited by freely-swimming fishes.

(Some figures may appear in colour only in the online journal)

1. Introduction

Recent advances in understanding undulatory fish locomotion, in which wave-like motions of the body generate propulsive forces, have included the use of robotic flapping foil devices which exhibit a rich variety of dynamic behaviors similar to the undulatory motions of live swimming fish (e.g., Triantafyllou *et al* 2000, Lauder 2011). The analysis of flapping models swimming under controlled conditions has attracted mathematicians (Alben *et al* 2012), fluid engineers (Anderson *et al* 1998, Buchholz and Smits 2008, Read *et al* 2003, Techet 2008), roboticists (Barrett *et al* 1999, Wen *et al* 2012, Low and Chong 2010) and biologists (Blevins and Lauder 2013, Fish *et al* 2006, Lauder and Madden 2006) interested in studying the principles underlying unsteady locomotion in aquatic animals. Recent work has included the study of passive flexible swimming foils which produce movements generally similar to swimming fishes to mimic undulatory body motion (Lauder *et al* 2007, 2011a, 2011b, Oeffner and Lauder 2012).

These recent studies tend to emphasize the locomotion of freely-moving foil models under self-propelled conditions.

This experimental method is both simple and useful for exploring a variety of topics in fish biomechanics, because it allows for direct quantitative comparisons of locomotor performance in terms of swimming speed, power consumption and wake flow among different models. Study of flapping foils under self-propulsion also ensures that time-averaged thrust and drag forces are in balance, and that the dynamics of swimming flexible foils generally mimic that of freely-swimming fishes.

However, one significant difference exists between current flapping foil models of fish propulsion and the locomotion of freely-swimming fishes: in fishes the center of mass oscillates axially during each tail beat cycle, while in current flapping foil models such axial oscillations are negligible due to the inertia of the motors and carriage used to drive the flapping heave and pitch motions. Masses of the driving carriage and motors can exceed that of the foil by one to two orders of magnitude, and as a result flapping motions of the swimming foils do not result in within-beat axial motion. Fishes swimming steadily in a time-averaged sense still exhibit center of mass oscillations (e.g., Tytell 2007, Walker 2004, Walker and Westneat 1997; Xiong and Lauder, unpublished data) in both vertical (up-down) and axial (streamwise) directions within each fin or tail beat cycle, and neither of these motions are currently modeled by flapping foil systems. Vertical oscillations are often caused by paired pectoral fins which move up and down in a flapping motion (Drucker and Lauder 1999), while axial oscillations in the fish center of mass are caused by the time-dependent thrust generation of either fins, the body or both. During self-propelled swimming by fishes the instantaneous forces acting on the body are not zero at each time step within an undulatory cycle: axial thrust forces periodically overwhelm the axial drag force during one beat as the body bends, resulting in an axial oscillation in both displacement and force. Averaged over a single flapping cycle, however, the mean axial force is zero when a fish is steadily swimming. Such axial oscillations in the center of mass are also nicely demonstrated in computational fluid dynamic models of unrestrained undulatory locomotion (e.g., Borazjani and Sotiropoulos 2008, 2009, Kern and Koumoutsakos 2006, Tytell *et al* 2010).

What effect does axial oscillation have on the dynamics of fish-like locomotion produced by flexible swimming foils? How does axial oscillation affect the kinematics and hydrodynamics of swimming? Can we use a robotic device to mimic the axial oscillation of freely-swimming objects and is there an optimal oscillation phase and amplitude? To test that, we must compensate for the large inertia of the flapper driving mechanism to enable the low-inertia flexible swimming foil to oscillate axially in the same way that a freely-swimming self-contained object would do in open water. To our knowledge, no experimental studies have yet addressed this issue in the field of fish biomechanics and robotics.

In this paper we use a robotic flapping foil system with a linear motor to produce precisely-controlled axial movements of the flapper carriage and motors as well as the swimming flexible foil. This modified design adds axial oscillation capability to the apparatus that we have used previously to study flexible foil propulsion (Lauder *et al* 2007, 2011a, 2011b, Oeffner and Lauder 2012).

To study how axial oscillations affect the kinematics and hydrodynamics of fish-like locomotion, we employed four plastic foil models of different lengths and flexural stiffnesses to achieve kinematic patterns similar to those two swimming fishes, eels (*Anguilla rostrata*) and bluegill sunfish (*Lepomis macrochirus*). We also simultaneously measured the force, kinematics, power and wake flow of the undulating foils. Finally, we discuss the implications of this inertia-compensated experimental method for robotic studies of undulatory locomotion, and the biological relevance of our experimental results.

2. Materials and methods

2.1. Time-averaged zero force self-propelling device

The experimental apparatus used a carriage containing a heave motor mounted on two low-friction air bearing rails above a recirculating flow tank (figure 1(*a*); also see Alben *et al* 2012, Lauder *et al* 2007, 2012 for previous work with this system). An encoder on the heave motor provided data on lateral position, while a linear encoder mounted on the carriage was used to gather the upstream and downstream position data for the foil. An ATI Nano-17 six-axis force/torque transducer (ATI Industrial Automation Inc., USA) was attached to a cylindrical shaft and allowed for three forces and three torques to be measured in the *XYZ* coordinate plane. The flexible plastic foil was attached via a stainless steel rod to the force transducer and submerged at mid-depth in the water tank.

A coherent, continuous beam 8 W argon-ion laser was used to generate a light sheet approximately 200 mm wide that intersected the middle of the foil (figures 1(*a*) and (*c*)). The flow tank was seeded with small, nearly neutrally-buoyant particles with diameter of 0.012 mm, and the image sequences of the flow were obtained using two Photron high-speed digital video cameras (Photron Inc., USA). The foil carriage and motor encoders, shaft forces and torques, and particle image videos were synchronized and data taken at the same sampling rate of 1000 Hz. Kinematics of the moving foils were digitized using Matlab. DaVis 7.2 software (LaVision Inc., UK) was used for particle image velocimetry analysis, as described in our previous studies (Lauder *et al* 2007, 2011a, 2011b, 2012). We digitized the leading and trailing edges of moving foils for all five replicate trials, and the results presented in table 2 are the averaged amplitude values. Midline kinematics were digitized from one representative trial as the motion was computer-controlled and highly repeatable.

We studied the swimming of two rectangular foils with two different thicknesses b and lengths L for a total of four foils (table 1). All foils had a uniform height (span) of $h =$ 68 mm. The flexural stiffness of the foil is defined by EI, where E denotes the Young's modulus and I indicates the foil second moment of area. For a simple rectangular foil with height h and thickness b, the second moment area of the foils I can be calculated by $I = hb^3/12$. The Young's modulus E of each foil material was measured using an Instron material testing machine (Instron, USA). In the present study, the two plastic materials we chose have different flexural stiffnesses of

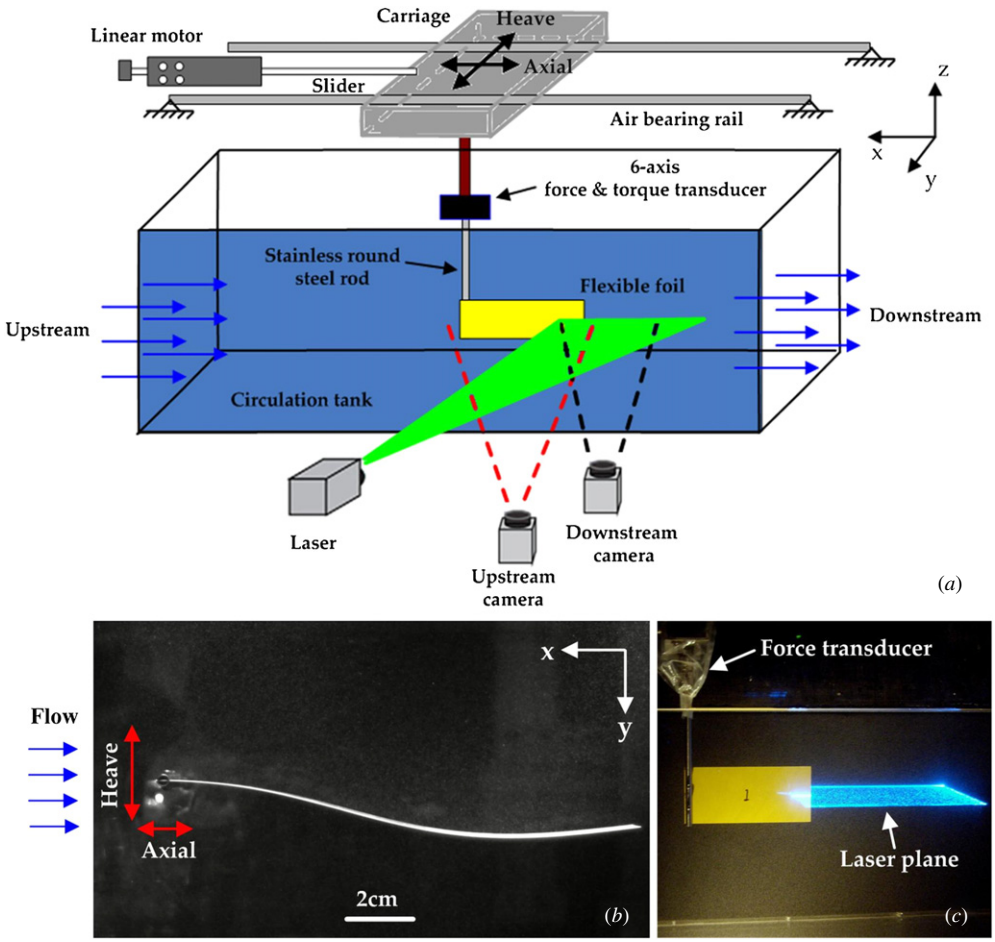

Figure 1. The robotic flapping foil apparatus. (*a*) Schematic view of the robotic experimental device over the recirculating flow tank. *x* points in the upstream-downstream direction, *y* points in the direction of heave and *z* points vertically up-down. The blue arrows indicate the direction of flow from upstream to downstream. The main mechanical components of the apparatus are indicated. (*b*) A ventral view snapshot of the swimming foil by high-speed cameras; the heave and axial directions are indicated by red arrows (the axial direction is parallel to the streamwise direction). (*c*) The flapping foil with the laser beam behind it to image wake flows.

Table 1. Shape and mechanical properties of foils A to D.

Foil	Foil length (mm)	Mass (g)	Flexural stiffness (Nm^2)	Thickness (mm)
A	150	32.1	9.9×10^{-4}	0.508
B	300	32.1	9.9×10^{-4}	0.508
C	150	32.1	3.3×10^{-5}	0.1
D	300	32.1	3.3×10^{-5}	0.1

$3.3 \times 10^{-5}\,Nm^{-2}$ and $9.9 \times 10^{-4}\,Nm^{-2}$ (table 1). According to literature values for reported values for the stiffnesses of freshly dead fish, the stiffnesses of these plastic foils falls within the range of those of fishes (see Lauder *et al* 2011b, Long *et al* 2002, McHenry *et al* 1995). We also tested two different lengths (L) of foils, so as to achieve different body wave numbers when the foils are in motion. Since the two foil types possessed different masses due to their differing thicknesses, we inserted small lead weights inside the foil shafts to bring each experimental condition to a common mass of 32.1 g (table 1). This ensured that inertial effects at the end of the oscillating shaft holding the foil were similar among the foil types.

The plastic foils were actuated with a heave (lateral, or side-to-side) motion at the leading edge according to

$$y = h_l \cos(2\pi f t), \tag{1}$$

where y denotes the heave motion of the foil in the lateral direction (figure 1(*b*)). In the current study, the mathematical amplitude (1/2 of the side-to-side trailing edge amplitude) of the heave motion in the lateral direction h_l was set at 1.5 cm. Flapping frequency f was set at 1.5 Hz. A Nano-17 force transducer (ATI Industrial Automation, Inc. USA; figure 1(*c*)) permitted measuring three forces (F_x, F_y, F_z) and three torques (T_x, T_y, T_z). In addition, the instantaneous fluid power consumption of the swimming foil P_{foil} can be calculated as

$$P_{\text{foil}} = F_y(\mathrm{d}y/\mathrm{d}t), \tag{2}$$

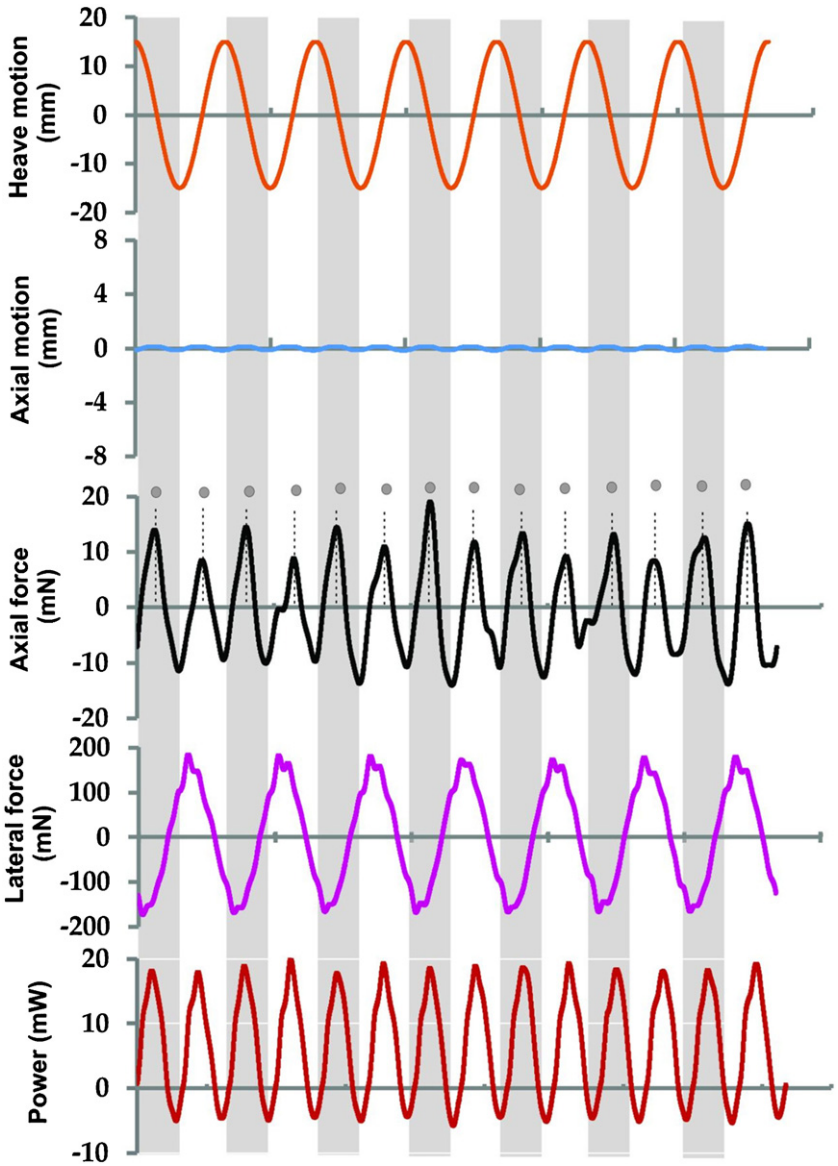

Figure 2. Sample data showing heave, axial motion of the foil leading edge, axial force, lateral force on foil A at its time-averaged self-propelled speed while heaving at $h_l = 1.5$ cm and $f = 1.5$ Hz ($U_{\mathrm{SPS}} = 195.1$ mm s^{-1}). From these data on foil motion and force, we calculate the instantaneous power, shown in the bottom graph. White and gray bars indicate half-cycles of flapping. The gray circles above the axial force indicate transient peaks of force during swimming.

where F_y denotes the measured lateral force along the heave direction.

The time-averaged self-propelled speed of the heaving foil was measured by adjusting the speed of the tank flow until the flapping robotic device generated sufficient thrust force to precisely hold still at a mean 'fixed' position (Lauder *et al* 2007, 2011a). The self-propelled speed of the swimming foils was then calculated in Labview (National Instruments, USA) from data collected by a series of swimming tests at a range of speeds (Lauder *et al* 2011a). Figure 2 shows sample data including foil heave motion and force and power data recorded from foil A at its self-propelled speed when actuated with $h_l = 1.5$ cm and $f = 1.5$ Hz at the leading edge. Thrust force and drag force were balanced over a flapping cycle when the foil moved at the constant self-propulsive speed (SPS): the time-averaged axial force was zero over each complete flapping cycle. The movement of the flapping foil under these conditions can be regarded as taking place in a time-averaged, self-propelled state.

2.2. Inertial-compensating method

Axial oscillation x of the flexible swimming foil should satisfy the following Newtonian equation:

$$m_f \frac{d^2x(t)}{\mathrm{d}t^2} = F_{x,\mathrm{ATI}}, \tag{3}$$

$F_{x,\mathrm{ATI}}$ denotes the axial force exerted by the fluid on the foil, and is measured by the ATI force transducer. x denotes the axial motion. We denote the mass of the plastic foil as m_f. The mass of foils A–D were equalized at 32.1 g so $m_f = 32.1$ g (table 1).

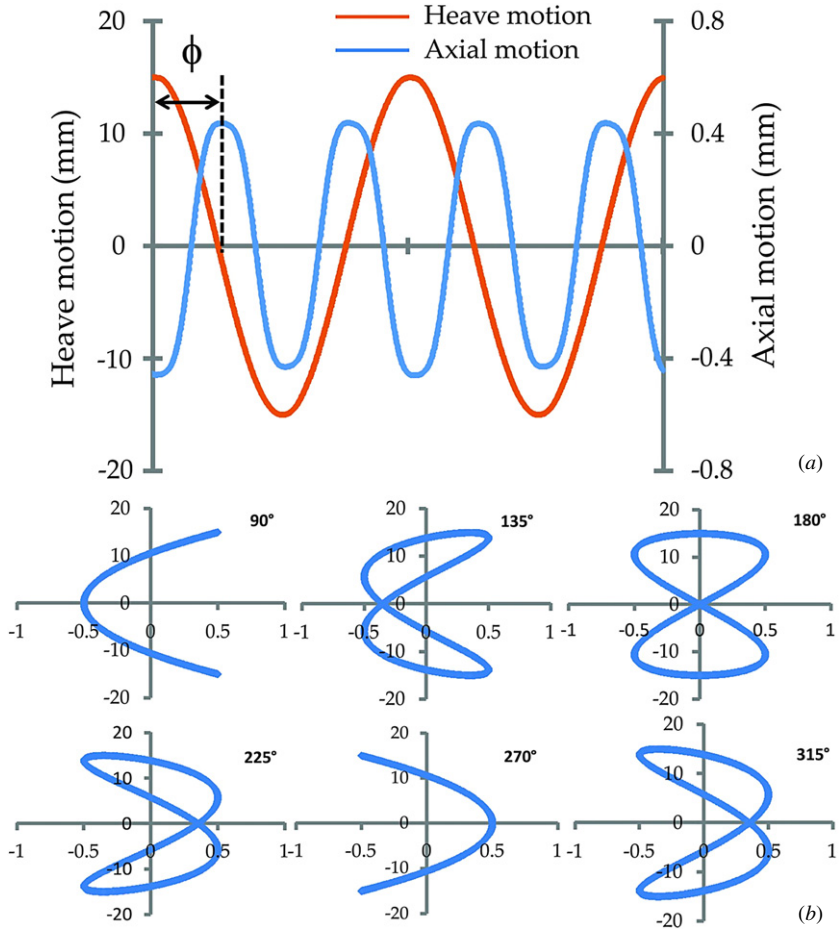

Figure 3. (*a*) The time history of axial and heave motions; φ indicates the phase between heave and axial movement. (*b*) Leading edge trajectories of the foil at different phases φ. For panel (*b*), both the *x*- and *y*-axis scales are in mm.

Without the addition of an inertial-compensating linear motor (discussed below), we measured the amplitude of axial carriage oscillation at approximately 0.05 mm when the foils were self-propelling. Why is the axial oscillation only 0.05 mm? With the whole carriage set on low-friction air bearings, the dynamics of the swimming foil satisfy the following:

$$(M_c + m_f)\frac{d^2x(t)}{dt^2} = F_{x,ATI}. \tag{4}$$

The components on the carriage include motors, air bearings and other parts of the mechanical drive system (Lauder *et al* 2007), which have a total mass of M_c. The carriage mass M_c is approximately 8 kg, which is much more massive than the plastic foil of 32.1 g: i.e. $M_c \gg M_f$. At self-propulsion, the axial forces produced by the swimming plastic foils are on the order of only 10 mN (figure 2), and such a small force cannot oscillate the heavy carriage axially to any significant extent.

To examine the effect of axial oscillations on swimming foils we used a linear motor system to provide appropriate axial motion to actively compensate for the inertia of the carriage and driving motors. We used a linear motor P01–23 × 160 controlled by E1100Gp (Linmot Inc., USA), with a movement repeatability of 0.05 mm, which allowed the axial motion to be accurately controlled. We then mounted the linear motor on the edge of the flow tank, and used a magnetic linear motor slider PL01-12 × 270/170 (Linmot Inc., USA) to push and pull the whole carriage set on the low-friction air bearing rails (figure 1(*a*)). A synchronizing trigger from the Labview control program allowed us to control the phase of linear motor axial oscillation with respect to foil heave motion, and synchronized axial foil motion, force and torque data acquisition, and image acquisition with two high-speed cameras for flow visualization.

The axial motion of the linear motor was programmed as follows:

$$x = h_a \sin(4\pi ft + \varphi), \tag{5}$$

where h_a indicates the amplitude of the axial oscillation, and φ is the phase difference between the axial and heave motions. As shown in figure 3(*a*), the axial motion was programmed to have twice the frequency of the heave oscillation. This is because the axial force in swimming foils oscillates at twice the frequency of the heave motion (see figure 2 for notation). Two axial force peaks during one flapping cycle have also been observed in previous studies of the unsteady cyclic motion of both swimming and flying animals (Triantafyllou *et al* 2005, Lauder *et al* 2011a, Sun and Wu 2003) and in computational analyses of fish undulatory propulsion (Borazjani and Sotiropoulos 2008, 2009). We also measured the mechanical time lag and

delay in stroke reversal of the linear motor slider including the mechanical connection to the carriage to be approximately 0.04 s. This backlash was then compensated for during data processing to obtain an accurate phase φ.

We used two methods to quantify how the axial motion affects fluctuations in the measured instantaneous axial force: root-mean-square (RMS), and average cyclic height (ACH). RMS for the instantaneous force measured over five cycles can be defined as:

$$\mathrm{RMS} = \sqrt{\frac{1}{5T}\int_0^{5T} (f(t))^2 \mathrm{d}t}. \quad (6)$$

In the current study, the ACH was also used to describe the average peak-to-peak axial force between the cyclic maxima and minima during five flapping cycles. Measurements of RMS and ACH were done using Labchart 7 (ADI Instruments Inc., USA).

In order to quantify how much inertial force was produced by the foil alone, we measured the inertial force generated in air by the axial motion in the absence of the heave motion with different linear motor programs. For these inertial force tests, we used a 'weight model' made of lead wire, with a mass equal to that of the foils (32.1 g) but with a very small surface area. In addition, we tested whether the axial force was 'contaminated' by the heave motion by heaving the inertial model at $f = 1.5$ Hz, $h_l = 1.5$ cm in the absence of any axial motion, i.e. the foil was held in place along axial direction. We found that the axial forces generated by the pure heave motion in air were negligible. In addition, the force measurements during the initial five flapping cycles were excluded from the analysis to allow the swimming foil to settle into a steady state.

3. Results

3.1. Instantaneous axial force

When the heave and axial motions were superimposed on the same graph, the leading edge trajectories show interesting patterns. Figure 3(*b*) shows the patterns of the leading edge trajectories at several phases of axial oscillation. The phase φ controls the shape of the pattern, while the amplitude h_a determines its width. By increasing the phase from 90° to 180°, the leading edge pattern gradually changes from a 'parabola' to a symmetrical '8' ('figure-eight') accordingly. Further increasing the phase to 270°, the pattern changes back to a parabola. At $\varphi = 135°$ and 225° the patterns resemble an asymmetrical figure-eight. To illustrate the dependence of the axial force fluctuation of the flapping foil ($f = 1.5$ Hz, $h_l = 1.5$ cm) as a function of the phase φ and amplitude h_a of linear motor program, we plot in figure 4 the variation of RMS and ACH for all foils and the instantaneous measured axial and inertial forces of foil A in figure 5.

We term the conditions of flapping foils that are self-propelled without axial motion as 'non-oscillated' states. In figure 5(*a*), when the foil A was heaved without axial motion ($h_a = 0, \varphi = 0$), the measured force showed two force peaks. In contrast, the instantaneous inertial force is nearly zero for the entire cycle. The hydrodynamic force generated by the flapping foil should be available to accelerate the foil either forward or backward once the foils are allowed to freely oscillate in the axial direction. However, at $h_a = 0$, the net hydrodynamic force is absorbed by the mechanical rod (figure 1(*a*)) without being compensated by the inertial force generated by the axial motion. As expected, RMS and ACH results of all foils A to D at 'non-oscillating' state are far from zero.

We found that axial motion significantly influences the instantaneous axial force. With addition of axial motion, at $h_a = 0.5$ mm, $\varphi = 0°$, the RMS and ACH were almost twice as large as those at $h_a = 0$ mm, $\varphi = 0°$ (figure 4). As φ increases, axial force gradually diminishes until a threshold at which both force RMS and ACH reach their lowest values (figure 4). The corresponding critical phases of foils for the minimal force fluctuation were marked by the dashed lines in figure 4. In figure 5(*b*), the instantaneous axial force at $\varphi = 270°$ and $h_a = 0.5$ mm is shown for foil A. Interestingly, at this phase the two hydrodynamic force peaks per flapping cycle almost vanish. In contrast, two clear force peaks appeared for the inertial force. However, as can be seen in figure 5(*c*), the instantaneous force is non-zero at $\varphi = 90°$. Further increasing the phase above the aforementioned critical phase also leads to larger force fluctuations (figure 4). We termed the phase at which the minimal force fluctuation occurs as the 'critical phase,' φ^*. This 'critical phase' can be observed for all foils with the addition of axial motion.

We then varied the amplitude h_a from 0 to 1 mm at the critical phase φ^* of each foil. As h_a increased, we found that the force fluctuation gradually decreased until reaching a 'critical amplitude,' $h_a{}^*$, at which force fluctuation reached a minimum. For example, in figure 4 foil A had a minimal force fluctuation at the corresponding critical amplitude $h_a{}^* = 0.425$ mm. Further increasing the amplitude above $h_a{}^*$ resulted in larger force fluctuation. For illustration, we plot the instantaneous force for $h_a = 1$ mm at $\varphi = 270°$ in figure 5(*d*), which demonstrates that the instantaneous measured axial force is far from zero again.

When the linear motor moves the foils axially at both 'critical' phases φ^* and amplitudes $h_a{}^*$, we termed those cases 'critically-oscillated' self-propelled states. Comparisons of foil force fluctuations, including RMS and ACH, in both 'non-oscillated' and 'critically-oscillated' states are shown in figures 5(*e*) and (*f*). Axial hydrodynamic force fluctuations were significantly reduced when foils were actuated axially at 'critically-oscillated' states.

Table 2 reports the critical phases φ^* and critical amplitudes $h_a{}^*$ for foils A to D, at which the minimum force fluctuations were obtained. The critical phases at self-propelled conditions occurred at 268°, 267.5°, 218° and 236°, for foils A to D, respectively. The critical amplitudes occurred at 0.43, 0.54, 0.49 and 0.44 mm, respectively. The time-averaged forces for all four foils remained at an average of zero at the 'critically-oscillated' self-propelled state.

3.2. Foil kinematics

Changing the lengths and flexural stiffnesses of foils resulted in different time-averaged self-propelled speeds U_{SPS} and foil midline kinematics. Increasing the foil length from 15 to 30 cm

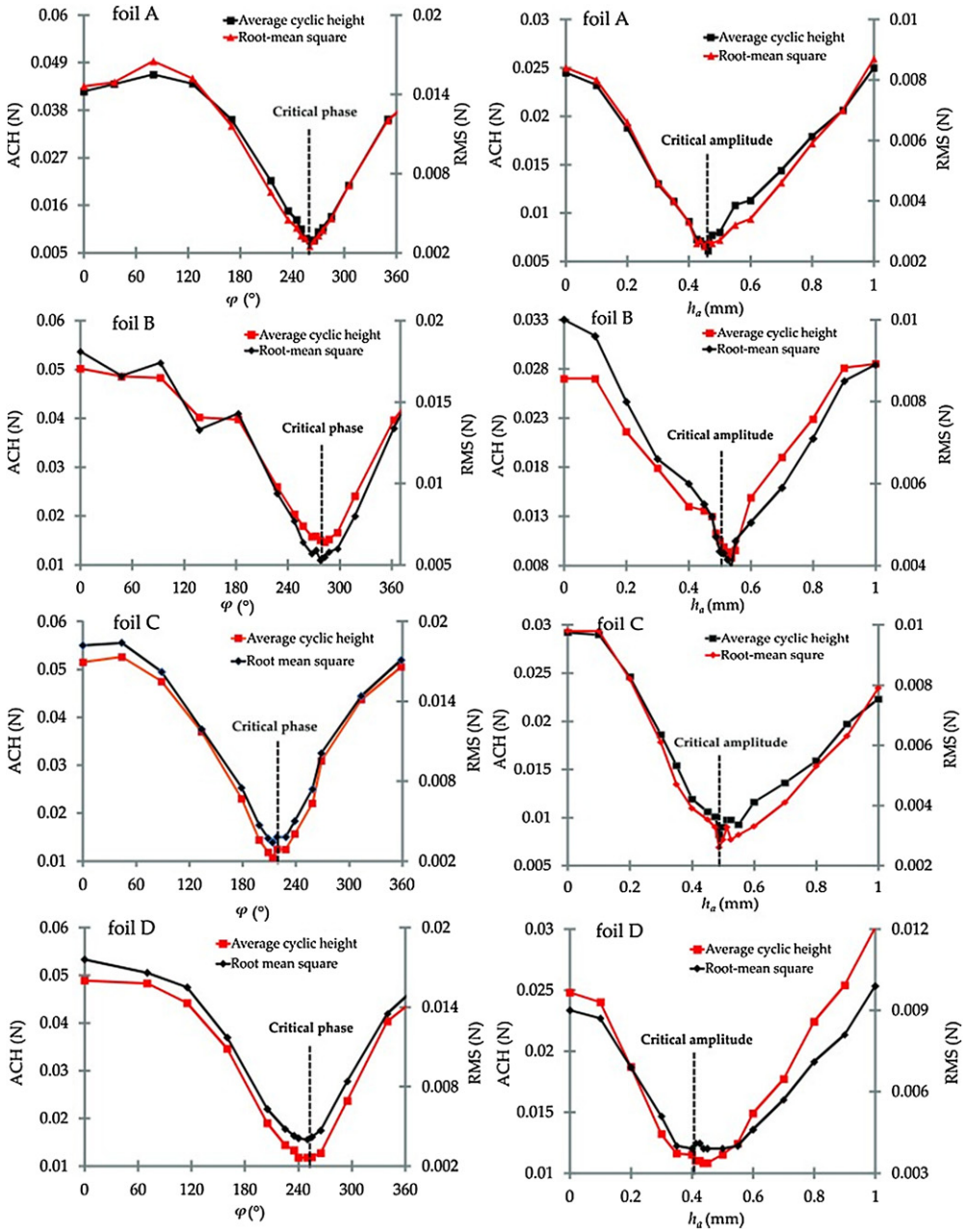

Figure 4. Root mean square (RMS) and average cyclic height (ACH) of force versus phase φ and axial oscillation amplitude h_a. The phase effect force tests were conducted at $h_a = 0.5$ mm; the amplitude effect tests were conducted at the 'critical phase' φ^*. The RMS and ACH of each point in the figures were averaged from five flapping cycles each for three separate individual tests.

Table 2. Kinematic data on foils A to D.

Variable	Abbreviation	Foil A	Foil B	Foil C	Foil D
Self-propelled speed (mm s^{-1})	*Usps*	195.1	210.4	162.3	175.0
Strouhal number	*St*	0.32	0.27	0.455	0.31
Wavelength (mm)	λ	345.5	423.5	190.9	206.0
Wave number	k	0.43	0.70	0.78	1.45
Critical amplitude (mm)	$h_a{}^*$	0.42	0.54	0.49	0.44
Critical phase (°)	φ^*	268.2	267.5	218.0	236.0
Axial speed oscillation (mm s^{-1})	*Urms*	4.0	5.1	4.6	4.1
Axial speed oscillation (%)	–	2.0%	2.4%	2.8%	2.3%
Trailing edge amplitude 'oscillated' (mm)	h_t	41.4	37.8	48.9	35.0
Trailing edge amplitude 'non-oscillated' (mm)	–	41.6	37.9	49.2	36.0

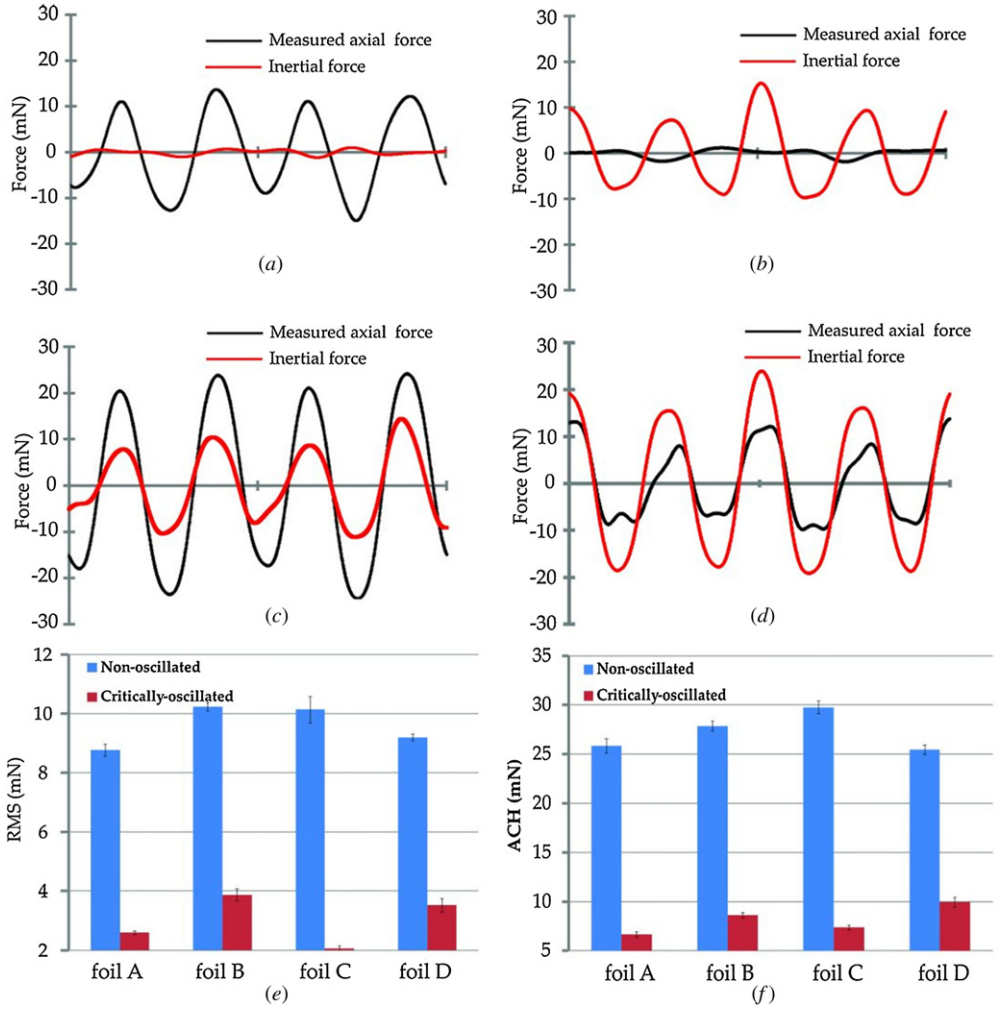

Figure 5. Instantaneous measured axial and inertial forces of foil A at different phases and axial amplitudes. (*a*) $h_a = 0$ mm, $\varphi = 0°$; (*b*) $h_a = 0.5$ mm, $\varphi = 270°$; (*c*) $h_a = 0.5$ mm, $\varphi = 90°$; (*d*) $h_a = 0$ mm, $\varphi = 0°$; Histograms of instantaneous measured axial forces: root mean square (RMS) results (*e*) and average cyclic height (ACH) (*f*) at both 'non-oscillated' and 'critically-oscillated' cases are provided (mean from $N = 3$ trials). Error bars are ± 1 s.e.m. All comparisons between oscillation modes are significantly different at $P < 0.0001$.

resulted in a relatively minor increase in swimming speeds of 7.6% and 7.8% for the soft and stiff foils, respectively (table 2). In contrast, for the same lengths, increasing the flexural stiffnesses of the foils caused an increase in swimming speed of 20.2% and 20.0%. The Strouhal numbers (*St*), which can be defined by $St = 2fh_t/U_{SPS}$, fell between the range of 0.27–0.45 for all foils, which is similar to that of live freely-swimming fishes. In general, the more flexible foils have a relatively shorter body wavelength λ and larger trailing edge amplitude h_t than the stiff foils. The wavelengths of the stiff flapping foils (A and B) are more similar to those found in the live swimming bluegill sunfish, and those of flexible foils (C and D) are more similar to swimming eels (figure 6). In table 2 we also report the speed oscillation U_{RMS}, which was obtained by taking the first derivative of the displacement of axial motion. The amplitudes of the speed oscillations of foils are between 4–5 mm s^{-1}, which are approximately 2%–2.5% U_{SPS} (time-averaged self-propelling speed). Trailing edge amplitudes of foils at both 'non-oscillated' and 'critically-oscillated' states used for the Strouhal number calculations are reported in table 2.

Body kinematics of a live freely-swimming eel (*A. rostrata*) and bluegill (*L. macrochirus*), which differ in mode of body undulation, are shown in figures 6(*a*) and (*b*). In figures 6(*c*) and (*d*), fish body midlines at equally-spaced time intervals throughout an undulating cycle are superimposed, and kinematics for distinct time instances are shown in different colors. In figures 6(*e*)–(*h*), we present the midlines of the swimming foils at 'critically-oscillated' states. These midline snapshots at the 'critically-oscillated' self-propelled foils are averages of three flapping cycles. Both the leading edges and trailing edges of foils moved in a figure-eight shape, and enlarged images of trajectories of the leading edge of the foils at the critically-oscillated state are shown in figure 7.

3.3. Wake flow and power consumption

Figures 8(*a*) and (*b*) show the wake flow generated by a steadily-swimming eel and bluegill sunfish, respectively (also see Tytell 2007). Figures 8(*c*)–(*f*) show flow visualization data from flexible foils C and D moving in both 'non-oscillated' and 'critically-oscillated' self-propelled states. Sets of staggered

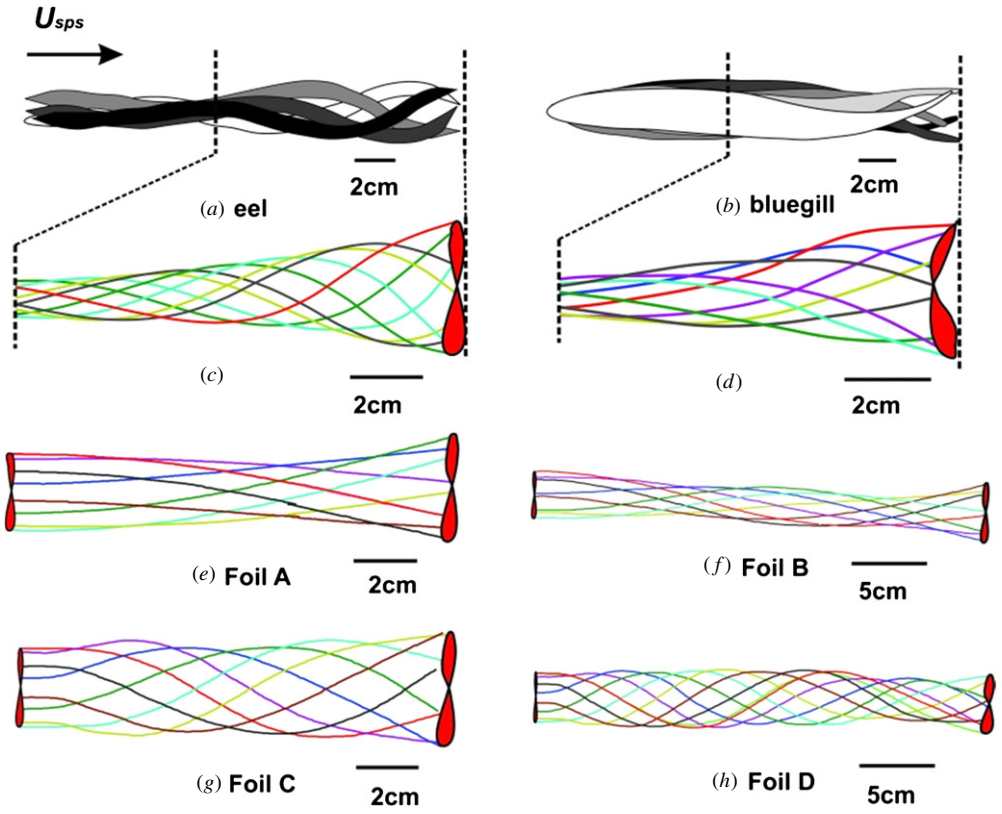

Figure 6. Body midlines of freely-swimming fishes and self-propelled foils at 'critically-oscillated' states (when minimal axial force fluctuations of foils were achieved) digitized from the ventral view. Eel (*A. rostrata*) and bluegill sunfish (*L. macrochirus*) outlines are shown in (*a*) and (*b*). In (*c*) and (*d*), body midlines at equally-spaced time intervals throughout a tail-beat are shown and aligned at the mid-body positions. Fish data are modified from (Lauder and Tytell 2006). Midline kinematics of foils A, B, C and D in the foils' 'critically-oscillated' states are shown in (*e*)–(*h*). The 'figure-eight' trajectories of the midline oscillations are filled with red at both leading edges and trailing edges for illustration. Enlarged leading edge trajectories for the foils are shown in figure 7.

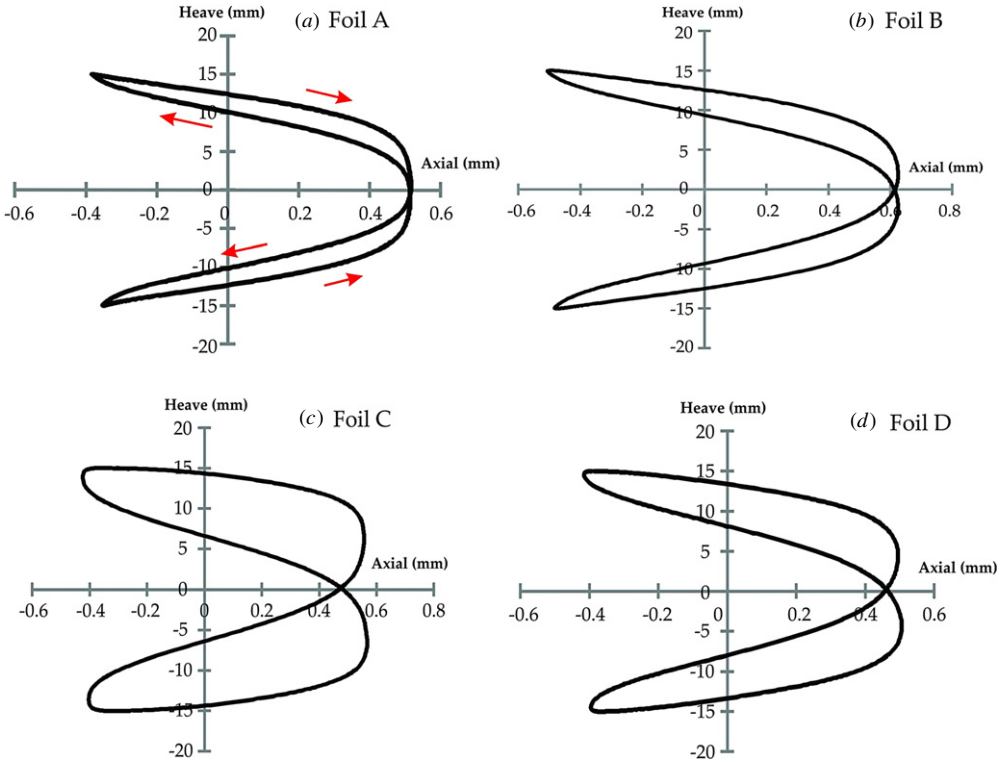

Figure 7. Enlarged leading edge trajectories of foil A (*a*), foil B (*b*), foil C (*c*) and D (*d*) at 'critically-oscillated' states. The trajectories of all foils move in 'figure-eight' patterns. The red arrows show the direction of the path in (*a*), and the rest of the foils have similar path directions.

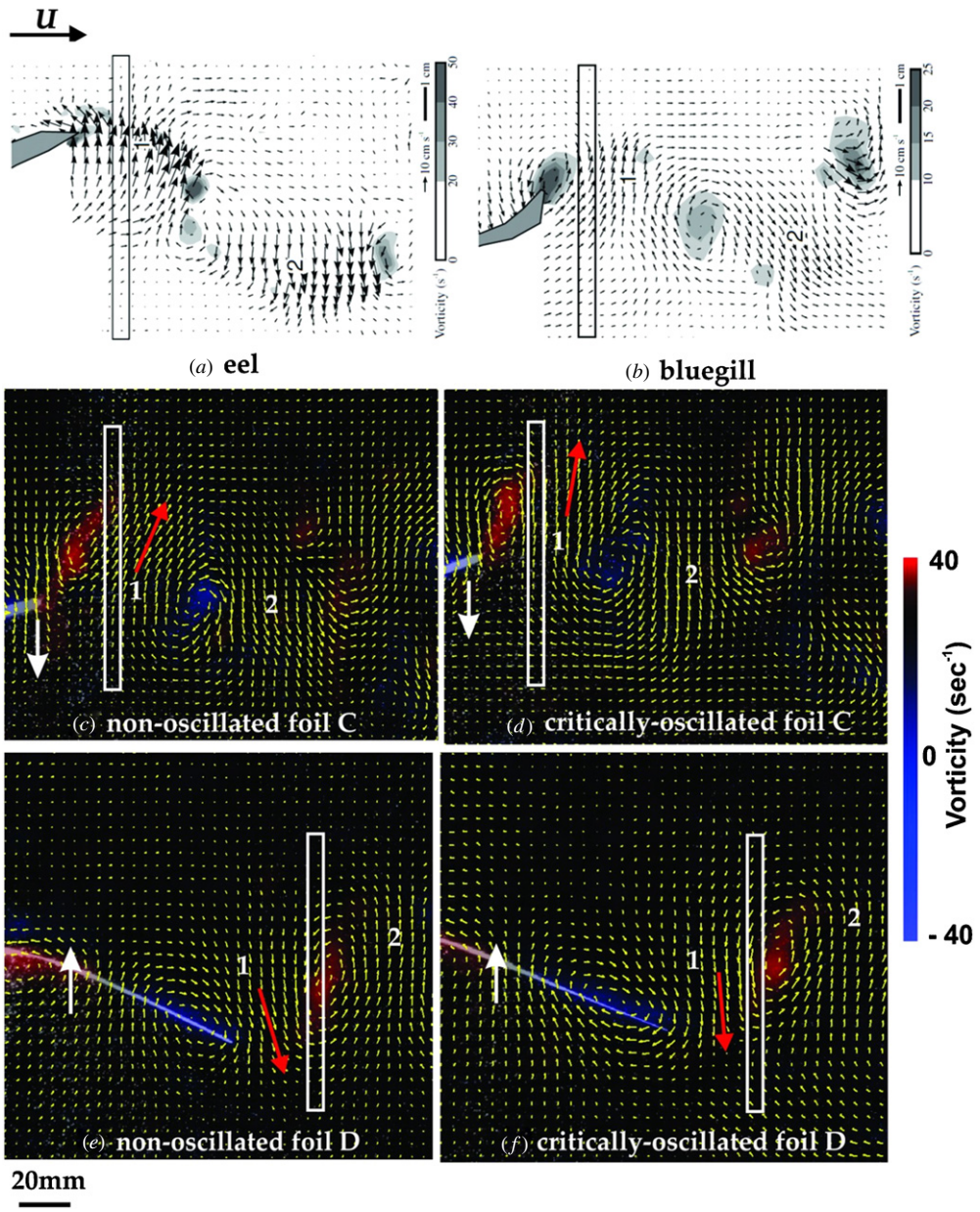

Figure 8. Flow visualization data on freely-swimming fishes and self-propelled foils. The particle image velocimetry (PIV) velocity vectors in the wake of a swimming eel (*A. rostrata*) and bluegill (*L. macrochirus*) are shown in (*a*) and (*b*). These data are modified from Tytell (2007). PIV velocity vectors of flexible foils C and D moving at both 'non-oscillated' and 'critically-oscillated' states at $t = T/2$ are shown in panels (*c*)–(*f*). White arrows indicate the direction of motion of the foil trailing edge. The major fluid jet flows are numbered as 1 and 2. Red arrows schematically represent the central jet flow in the wake (quantitative comparisons are provided in figure 10), and the jet angle α is defined relative to the flow direction (U). The position of velocity transects shown in figure 9 are indicated by a white box which is 5 mm wide and placed 20 mm downstream of the foil's trailing edge. Scale bars are shown below and are same for panels (*c*)–(*f*). Background flow velocities have been subtracted for the PIV vectors of both fishes and foils.

vortices are arrayed in the wake, with a higher velocity jet at angle α between them pointing laterally and in the axial direction. The wake generated by the foils is generally similar to that of the live fishes. When foil C moves at 'non-oscillated' state, the flow of the wake contains a jet with a relatively distinct axial component, at a mean α of 67.2° (figure 8(*c*)). The flow in the wake of foil A in the 'critically-oscillated' self-propelled state produced a mean jet angle of 78.3°, 16.5% larger than when the foil was at a 'non-oscillated' state. Figures 8(*c*) and (*d*) show the wake of foil D. The mean jet angle in the 'non-oscillated' state was 76.7°, and 82.7° at 'critically-oscillated' state.

Figures 9(*a*) and (*b*) show the average wake velocity profiles of eels and bluegill sunfish swimming steadily in a recirculating flow tank (from Tytell 2007). In the present study, we estimated the instantaneous net fluid velocity in a 5 mm thick box placed 20 mm downstream from the foil trailing edges, as can be seen in figure 8. In figure 9, the wake transects were obtained by averaging PIV velocity vectors along the axial dimension of the boxes for comparison to the wake profiles of swimming fishes.

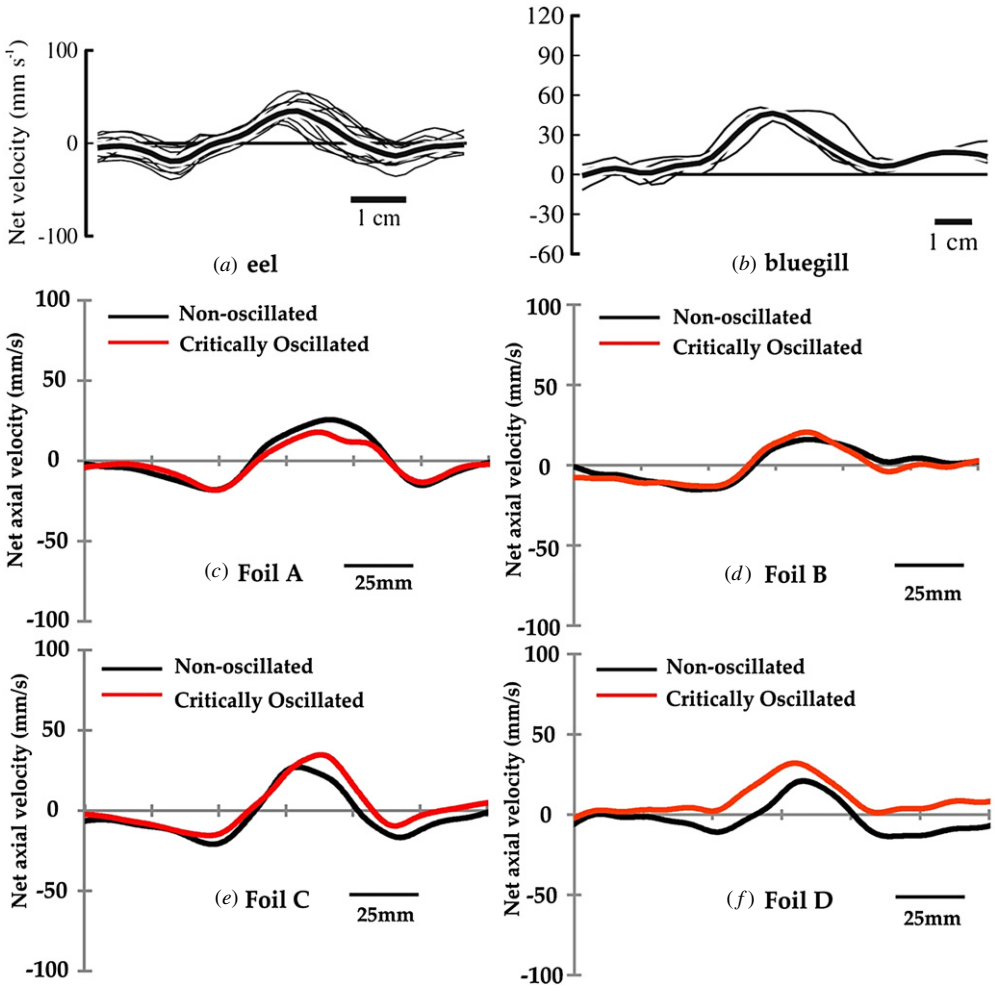

Figure 9. Transects of average axial wake velocity 10 mm downstream of swimming fishes (*a*) eel (*A. rostrata*), and (*b*) bluegill sunfish (*L. macrochirus*) (data modified from Tytell 2007), and foils both 'non-oscillated' and 'critically-oscillated' cases: (*c*) Foil A; (*d*) Foil B; (*e*) Foil C; (*f*) Foil D. The length of the wake profiles of the foils is 150 mm spanning from left to right.

For the stiffer foils (A and B), the *mean* wake velocities in both 'non-oscillated' and 'critically-oscillated' states are nearly zero. The average wake velocities of foils A and B showed profiles that have center peaks with speeds above zero, and two side lobes with speeds below zero. It can be seen in figures 9(*c*) and (*d*) that the average wake profiles in both cases almost overlap. Thus, we speculate that axial oscillation has very little effect on the wake flow of the stiffer foils used in the present study. In contrast, the average flow velocity of more flexible foil C in the 'critically-oscillated' state was slightly smaller than that of the foil in the 'non-oscillated' state. Interestingly, the mean flow velocity when not oscillated was 7.4 mm s^{-1} larger than when the longer flexible foil (foil D) was oscillated. This result is also reflected in figure 9(*f*), where the wake profile of foil D is clearly above zero: the average flow velocity is about 5.7% of the self-propelled speed.

The jet angles of the wakes of foils A to D in both 'non-oscillated' and 'critically-oscillated' states are shown in figure 10(*a*). The instantaneous wake flows of foils A and B at 'non-oscillated' and 'critically-oscillated' states are not presented in figure 8 because they are not significantly different according to the statistical analysis (figure 10(*a*)).

We also consider how much power P_{foil} (see equation (2) for definition) is consumed by the foils. The stiffer foils (A and B) achieved faster self-propelled speeds, but consumed more power than the flexible foils (C and D). Power consumption increases about 28% by increasing the length of the stiff foils from 15 to 30 cm. For the flexible foils, however, power only increased 0.6% as the length doubled. In addition, stiffer foils consume more power than the flexible foils. Figure 10(*b*) shows that the difference in power requirements of foils at 'non-oscillated' and 'oscillated' self-propelled states is small and not significant, and axial oscillation thus did not affect power consumption of the swimming foils.

Wake profiles differ considerably among the swimming foils, and figure 11 shows the time-averaged flow field of foils A to D in 'critically-oscillated' self-propelled states. The averaged wake of the short foils (A and C) splits into two jet-like bifurcating streams, with local flow speed slightly greater than the incoming flow velocity (figures 11(*a*) and (*c*)). For longer foils, as shown in figures 11(*b*) and (*d*), the averaged flow field showed a relatively narrow high velocity wake region. In general, the current results demonstrate that the wake flow of the foils at 'critically-oscillated' self-propelled

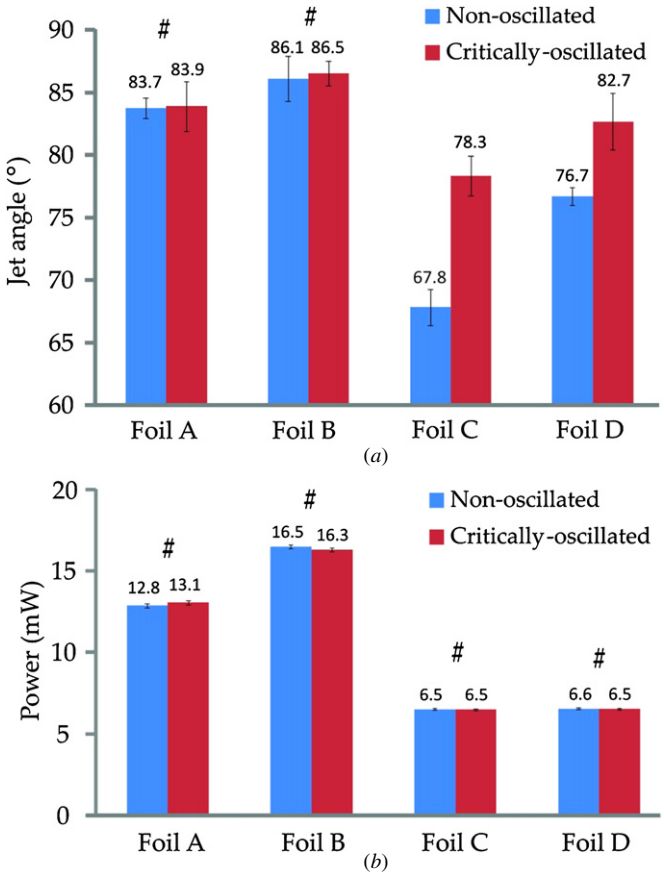

Figure 10. Jet angle (*a*) and mean power consumption (*b*) of self-propelled foils in 'non-oscillated' and 'critically-oscillated' states. Error bars are ± 1 s.e.m. Within each group of similarly-colored bars, bars with # symbols above are not significantly different from each other ($P > 0.05$), while other comparisons have a level of significance $P < 0.05$.

states have very small average net axial velocities, which is close to a time-averaged 'non-momentum' wake.

4. Discussion

4.1. The 'inertia-compensated' self-propelled method

When fishes swim freely in the aquatic environment, their center of mass oscillates within each tail beat cycle. Even though when fish swim steadily with a time-averaged within-cycle force of zero, the instantaneous forces experienced by the center of mass are not zero, and oscillate at twice the tail beat frequency in the axial direction. But previous robotic flapping foil models using both rigid and flexible foils have not allowed within-cycle axial motion, and the effect of such motions on locomotor dynamics is unknown. In this paper our goal was to implement a control system that allows us to generate foil oscillation in the streamwise direction, and to alter the phase and magnitude of this oscillation. This addition to the robotic flapping foil apparatus allows consistent flapping motion inputs (frequency and heave amplitude) for the foils swimming in either 'non-oscillated' states or controllable oscillated states. In contrast to experiments conducted with live fishes, which are always freely-swimming with axial oscillations (Tytell 2007), this robotic apparatus allows us to alter axial oscillation parameters experimentally and determine if there is a phase and amplitude of axial oscillation that minimizes force oscillations on the center of mass.

We found that there are indeed 'critically-oscillated' states, during which axial force fluctuations were minimized to nearly zero for foils with different lengths and flexural stiffnesses, and when most of the axial instantaneous hydrodynamic force was compensated for by inertial forces. By comparing hydrodynamics of foils in both 'non-oscillated' and 'critically-oscillated' states, we found that the axial oscillations had an impact on the wake flow of flexible foils but had little effect on stiffer foils (figures 9(*c*) and (*d*) and 10(*a*)). Thus, when studying the kinematics and hydrodynamics of self-propelling foils with greater stiffness it is reasonable to neglect axial oscillations, but the axial oscillations of flexible foils have a substantial impacts on locomotor dynamics.

Comparison of force oscillations between 'critically-oscillated' and 'non-oscillated' states shows that we were able to suppress most of the axial force oscillation (figures 5(*e*) and (*f*)). But a small amount of 'residual force' still exists when the undulatory foils oscillated even at a 'critically-oscillated' state. We speculate that this is due to the fact that the foils do not undulate perfectly symmetrically. Making the left and right strokes of flexible flapping foils perfectly symmetrical was not possible and there were inevitably small asymmetries in foil motion. Axial force will then become slightly non-zero due to any small deviation from a symmetrical flapping stroke. However, the 'critically-oscillated' state resulted in a minimal force fluctuation which is very close to zero, and we believe that we can take the 'critically-oscillated' state of the swimming foils as representative of 'instantaneous' self-propulsion, which has an axial force of nearly zero at every instant like a freely-swimming fish. At this condition, the amplitude of the imposed axial oscillation should approximate the amplitude of the center of mass motion seen if the foils were swimming unattached and isolated from driving masses, under their own power.

4.2. Axial oscillation of self-propelling foils and freely-swimming fishes

The trajectory of the leading edges of these flexible foils moved in a figure-eight shape at 'critically-oscillated' states (figure 7). As mentioned earlier, the difference in leading edge movement pattern is due to the phase φ between heave motion and axial motion. Specifically, our results show that the kinematics of the leading edges of stiffer foils at 'critically-oscillated' states generated patterns shaped like parabolas, while the flexible foils moved in pattern shaped more like a figure-eight (figure 7). In addition, the width of the pattern is determined by the amplitude h_a. Using different physical foil models with a uniform mass of 32.1 g, we found that the peak-to-peak axial oscillation at 'critical-oscillated' states are all very nearly 1 mm (twice the critical amplitude value given in table 2).

Live fish also have axial oscillations, although quantifying the amplitude of these oscillations during undulatory

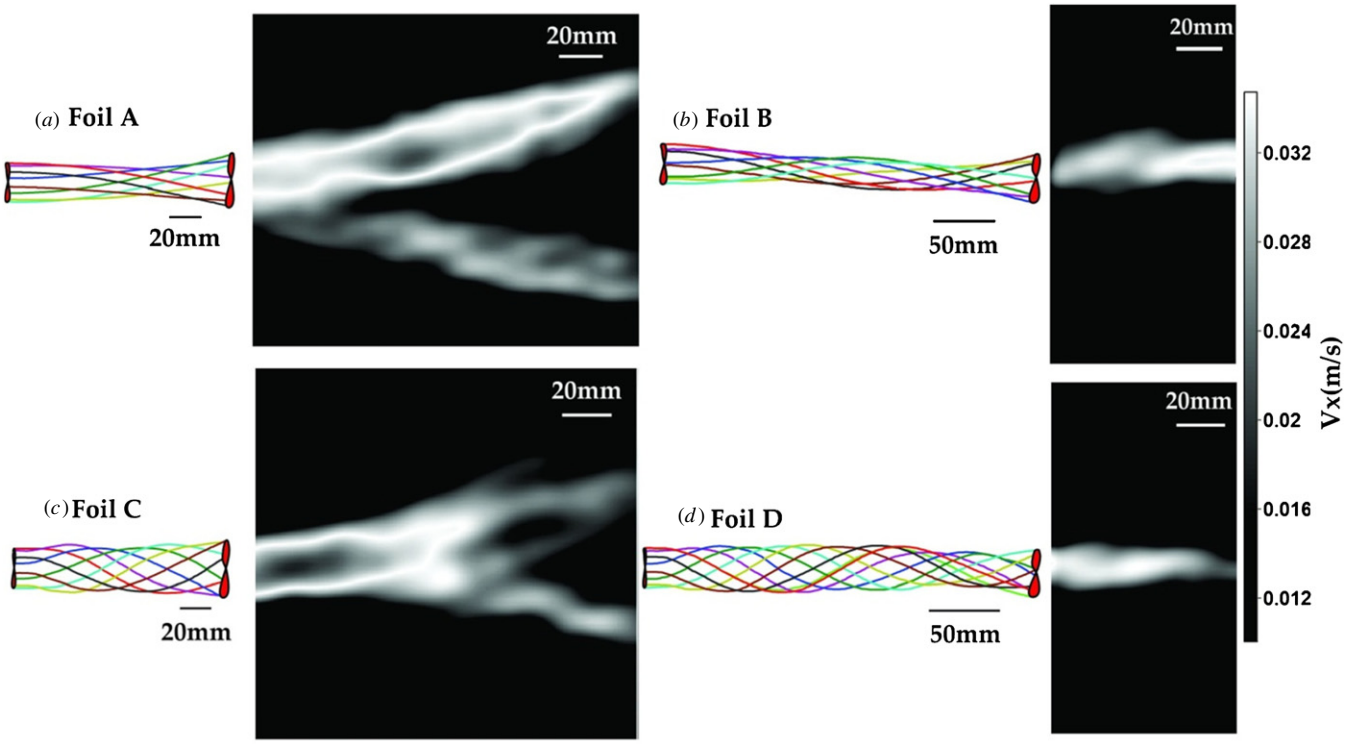

Figure 11. Time-averaged axial wake velocity fields in 'critically-oscillated' states for self-propelling foils (*a*) Foil A; (*b*) Foil B; (*c*) Foil C; (*d*) Foil D. Flow direction is from left to right. White color indicates relatively high axial wake flow velocity, black color indicates zero wake velocity. Note the bifurcating wake for the two shorter foils.

propulsion has proven to be quite challenging (Tytell 2007). Recently obtained data in our laboratory for center of mass oscillations during undulatory locomotion in several fish species suggests that the peak-to-peak axial oscillations range from 0.5 to 1.5 mm depending on species and speed (Xiong and Lauder, unpublished data) for fishes of similar surface area to the foils studied here. These values correspond well with the mean peak-to-peak values of critical axial oscillation found here for the flexible foils: 0.93 mm averaged across all four foils.

4.3. Hydrodynamics of self-propelling foils and freely-swimming live fishes

At 'critically-oscillated' self-propelling states, we found that the wake jet angles were 83.9° and 86.5° for short and long stiff foils, while the jet angles were 78.3° and 82.7° for short and long flexible foils (figure 10(*a*)). According to the average wake profiles (figure 9), we found that stiff foils produce almost zero mean axial net velocity, but flexible foils produce some net positive velocity. A self-propelled, two-dimensional foil should ideally generate a jet angle with 90° and zero mean axial net velocity, indicating a balanced time-averaged thrust and drag forces (Tytell 2007). A jet angle of 0° means the entire jet is producing thrust force, while an angle of greater than 90° produces a completely lateral force with zero mean axial net velocity (Meunier and Spedding 2006).

When comparing self-propelling flexible foils of different lengths, complex resonant effects can be observed that may complicate simple interpretations of the effects of length changes. For example, Alben *et al* (2012) and Lauder *et al* (2012) illustrate experimentally and with an analytical model that flexible flapping foils can exhibit substantial changes in swimming speed as a result of even small length changes. And the relationship between self-propelled swimming speed and foil length changes with the stiffness of the foil, further complicating simple comparisons.

According to the time-averaged flow analysis, we found that the bifurcating wake generated by the shorter foils (figures 11(*a*) and (*c*)) is notably different from the more jet-like narrow wake behind the longer foils (figures 11(*b*) and (*d*)). Bifurcating wakes have not to our knowledge been previously reported in fish-like undulatory swimming of flexible foils, although the papers by Dong *et al* (2006) and Dewey *et al* (2012) show a bifurcating wake under certain conditions in their studies of both rigid and stingray-like actuated pitching panels respectively. The significance of the bifurcating wake structure for locomotor dynamics of fish-like undulatory swimming is as yet unknown.

Nauen and Lauder (2002) analyzed wake flow patterns produced by swimming chub mackerel (*Scomber japonicus*) and showed that the jet angle is $67 \pm 9°$ at a steady swimming speed of 1.2BL/s. Tytell (2007) also reported that time-averaged wakes of swimming trout and bluegill have jet angles that are less than 90°, and the mean net flow velocities are around 2% and 5% greater than the time-averaged steady swimming speed (*Usps*). In contrast, the eel wake consists of jets of fluid that point almost laterally (figure 8(*a*)), and the jet angle reaches up to 89° (Tytell and Lauder 2004) with the mean axial net velocity approaching zero (Tytell 2007).

Why are wake jet angles not 90° and why does a positive mean axial net velocity exist for freely-swimming live fishes (except eels) and the robotic foils studied here? We speculate that it is possibly due to the fact that there might be a contribution to the net thrust force produced by the undulatory anterior part of the fish or flexible foils. For example, leading edge suction on the body or fins can contribute substantially to trust and has been demonstrated previously in flexible foil propulsion (Borazjani and Daghooghi 2013, Oeffner and Lauder 2012). In addition, complicated three-dimensional effects arising from the fins and body edges above and below the laser plane in which flows are visualized here almost certainly play a role in contributing to the wake flow field and momentum transfer from the fish or foil to the fluid. To better understand this issue, further numerical and experimental three-dimensional flow analyses around both freely-swimming live fish and robotic foil models are needed (e.g., Borazjani and Daghooghi 2013, Flammang *et al* 2011).

One noteworthy aspect of the self-propelling passively flexible foils is that their kinematics closely approximate the posterior thrust producing region of undulatory fish locomotion (e.g., figure 6). We believe that there are several reasons for this. First, during slow to moderate swimming speeds, fish activate only red muscle fibers which make up only a small fraction (less than 10%) of the fish's muscle mass. Most of the body, composed of myotomal white fibers, is thus acting passively. Second, during a number of fish swimming behaviors, including locomotion behind bluff bodies that shed a Karman vortex street, fish can generate thrust with a passive flexible body (Beal *et al* 2006, Liao *et al* 2003a, 2003b), and passive body dynamics are critical to swimming in the Karman vortex street. Third, over a wide range of swimming speeds, the anterior body region of swimming fish undergoes minimal heave motion, and it is the posterior body that is the thrust generating region (Lauder and Tytell 2006). This area is thus well modeled by a flapping flexible foil that generates thrust as a result of heave motion at its leading edge, and the passive flexible foils studied here show curvatures that are similar to those of freely-swimming fishes.

5. Conclusions

We provide an analysis of the swimming performance of undulating passive robotic foils with axial oscillation that is biologically relevant to freely-swimming fish by flapping plastic foils with two different lengths and two stiffnesses. We found 'critically-oscillated' states for each foil when the axial force fluctuation reached a minimum, and when most of the instantaneous hydrodynamic forces were compensated by inertial forces. While at 'critically-oscillated' states, the foils with biologically relevant heave parameters resulted in ~1 mm total oscillation in the axial direction, similar to recently obtained results on center of mass oscillations from freely-swimming fishes. At 'critically-oscillated' states, the leading edge patterns of flexible foils are figure-eight-shaped, while the motion of the leading edge of stiffer foils is shaped more like a parabola. From flow visualization analyses, some differences in wake flow patterns were observed in flexible foils between the 'critically-oscillated' and 'non-oscillated' states. Axial oscillation thus affects swimming hydrodynamics of flexible bodies, but has much less effect on stiff foils.

The addition of a mechanism that generates controlled axial oscillations to current robotic foil systems provides a new experimental avenue for studying the dynamics of self-propelled swimming in flexible bodies.

Acknowledgments

This work was supported by NSF grant EFRI-0938043. We thank members of the Lauder and James Tangorra Labs (Drexel University) for many helpful discussions on fish fins and flexible flapping foil propulsion, Silas Alben for assistance in interpreting flapping foil results, Eric Tytell for many discussions on wake flow patterns, Dan Quinn for discussing the force and wake results, Erik Anderson, Vern Baker, and Chuck Witt for their considerable efforts in designing the robotic flapper and control software, and Erin Blevins and Gabe Walker for improving the paper.

References

Alben S, Witt C, Baker T V, Anderson E J and Lauder G V 2012 Dynamics of freely swimming flexible foils *Phys. Fluids* A **24** 051901

Anderson J M, Streitlien K and Barrett D S 1998 Oscillating foils of high propulsive efficiency *J. Fluid Mech.* **360** 41–72

Barrett D S, Triantafyllou M S and Yue D P 1999 Drag reduction in fish-like locomotion *J. Fluid Mech.* **392** 183–212

Beal D N, Hover F S, Triantafyllou M S, Liao J and Lauder G V 2006 Passive propulsion in vortex wakes *J. Fluid Mech.* **549** 385–402

Blevins E and Lauder G V 2013 Swimming near the substrate: a simple robotic model of stingray locomotion *Bioinspir. Biomim.* **8** 016005

Borazjani I and Daghooghi M 2013 The fish tail motion forms an attached leading edge vortex *Proc. R. Soc. Lond. Biol. Sci.* **280** 20122071

Borazjani I and Sotiropoulos F 2008 Numerical investigation of the hydrodynamics of carangiform swimming in the transitional and inertial flow regimes *J. Exp. Biol.* **211** 1541–58

Borazjani I and Sotiropoulos F 2009 Numerical investigation of the hydrodynamics of anguilliform swimming in the transitional and inertial flow regimes *J. Exp. Biol.* **212** 576–92

Buchholz J H and Smits A J 2008 The wake structure and thrust performance of a rigid low-aspect-ratio pitching panel *J. Fluid Mech.* **603** 331–65

Dewey P A, Carriou A and Smits A J 2012 On the relationship between efficiency and wake structure of a batoid-inspired oscillating fin *J. Fluid Mech.* **691** 245–66

Dong H, Mittal R and Najjar F M 2006 Wake topology and hydrodynamic performance of low aspect-ratio flapping foils *J. Fluid Mech.* **566** 309–43

Drucker E G and Lauder G V 1999 Locomotor forces on a swimming fish: three-dimensional vortex wake dynamics quantified using digital particle image velocimetry *J. Exp. Biol.* **202** 2393–412

Fish F, Nusbaum M, Beneski J and Ketten D 2006 Passive cambering and flexible propulsors: cetacean flukes *Bioinspir. Biomim.* **1** S42–8

Flammang B E, Lauder G V, Troolin D R and Strand T 2011 Volumetric imaging of fish locomotion *Biol. Lett.* **7** 695–98

Kern S and Koumoutsakos P 2006 Simulations of optimized anguilliform swimming *J. Exp. Biol.* **209** 4841–57

Lauder G V 2011 Swimming hydrodynamics: ten questions and the technical approaches needed to resolve them *Exp. Fluids* **51** 23–35

Lauder G V, Anderson E J, Tangorra J and Madden P G A 2007 Fish biorobotics: kinematics and hydrodynamics of self-propulsion *J. Exp. Biol.* **210** 2767–80

Lauder G V, Flammang B E and Alben S 2012 Passive robotic models of propulsion by the bodies and caudal fins of fish *Integr. Comp. Biol.* **52** 576–87

Lauder G V, Lim J, Shelton R, Witt C, Anderson E and Tangorra J L 2011a Robotic models for studying undulatory locomotion in fishes *Mar. Technol. Soc. J.* **45** 41–55

Lauder G V and Madden P G A 2006 Learning from fish: kinematics and experimental hydrodynamics for roboticists *Int. J. Automat. Comput.* **4** 325–35

Lauder G V, Madden P G, Tangorra J L, Anderson E and Baker T V 2011b Bioinspiration from fish for smart material design and function *Smart Mater. Struct.* **20** 094014

Lauder G V and Tytell E D 2006 Hydrodynamics of undulatory propulsion *Fish Biomechanics. Volume 23 in Fish Physiology* ed R E Shadwick and G V Lauder (San Diego, CA: Academic) pp 425–68

Liao J, Beal D N, Lauder G V and Triantafyllou M S 2003a The Kármán gait: novel body kinematics of rainbow trout swimming in a vortex street *J. Exp. Biol.* **206** 1059–73

Liao J C, Beal D N, Lauder G V and Triantafyllou M S 2003b Fish exploiting vortices decrease muscle activity *Science* **302** 1566–9

Long J, Koob-Emunds M, Sinwell B and Koob T J 2002 The notochord of hagfish *Myxine glutinosa*: visco-elastic properties and mechanical functions during steady swimming *J. Exp. Biol.* **205** 3819–31

Low K H and Chong C W 2010 Parametric study of the swimming performance of a fish robot propelled by a flexible caudal fin *Bioinspir. Biomim.* **5** 046002

McHenry M J, Pell C A and Long J H 1995 Mechanical control of swimming speed: stiffness and axial form in undulating fish models *J. Exp. Biol.* **198** 2293–305

Meunier P and Spedding G R 2006 Stratified propeller wakes *J. Fluid Mech.* **552** 229–56

Nauen J C and Lauder G V 2002 Hydrodynamics of caudal fin locomotion by chub mackerel, *Scomber japonicus* (*Scombridae*) *J. Exp. Biol.* **205** 1709–24

Oeffner J and Lauder G V 2012 The hydrodynamic function of shark skin and two biomimetic applications *J. Exp. Biol.* **215** 785–95

Read D A, Hover F S and Triantafyllou M S 2003 Forces on oscillating foils for propulsion and maneuvering *J. Fluid Struct.* **17** 163–83

Sun M and Wu J H 2003 Aerodynamic force generation and power requirements in forward flight in a fruit fly with modeled wing motion *J. Exp. Biol.* **206** 3065–83

Techet A H 2008 Propulsive performance of biologically inspired flapping foils at high Reynolds numbers *J. Exp. Biol.* **211** 274–79

Triantafyllou M S 2005 Review of hydrodynamic scaling laws in aquatic locomotion and fish-like swimming *Appl. Mech. Rev.* **58** 226–38

Triantafyllou M S, Triantafyllou G S and Yue D P 2000 Hydrodynamics of fishlike swimming *Ann. Rev. Fluid Mech.* **32** 33–53

Tytell E D 2007 Do trout swim better than eels? Challenges for estimating performance based on the wake of self-propelled bodies *Exp. Fluids* **43** 701–12

Tytell E D, Hsu C Y, Williams T L, Cohen A H and Fauci L J 2010 Interactions between body stiffness, muscle activation, and fluid environment in a neuromechanical model of lamprey swimming *Proc. Natl Acad. Sci.* **107** 19832–7

Tytell E D and Lauder G V 2004 The hydrodynamics of eel swimming: I. Wake structure *J. Exp. Biol.* **207** 1825–41

Walker J A 2004 Dynamics of pectoral fin rowing in a fish with an extreme rowing stroke: the threespine stickleback (*Gasterosteus aculeatus*) *J. Exp. Biol.* **207** 1925–39

Walker J A and Westneat M W 1997 Labriform propulsion in fishes: kinematics of flapping aquatic flight in the bird wrasse *Gomphosus varius* (Labridae) *J. Exp. Biol.* **200** 1549–69

Wen L, Wang T M, Wu G H and Liang J H 2012 Hydrodynamic investigation of a self-propulsive robotic fish based on a force-feedback control method *Bioinspir. Biomim.* **7** 036012